forests

MDPI

Article

Canopy Structural Complexity Buffers the Carbon–Water Trade-Off in Chinese Forests

Xiaofang Sun [1], Meng Wang [1] and Guicai Li [2,*] and Fengshan Liu [3]

[1] School of Geography and Tourism, Qufu Normal University, Rizhao 276800, China; sunxf@qfnu.edu.cn (X.S.); wangmeng@qfnu.edu.cn (M.W.)
[2] Key Laboratory of Radiometric Calibration and Validation for Environmental Satellites, National Satellite Meteorological Center (National Center for Space Weather), Innovation Center for Feng Yun Meteorological Satellite, Beijing 100081, China
[3] China National Engineering Research Center of JunCao Technology, International College of JunCao Science, Fujian Agriculture and Forestry University, Fuzhou 350002, China; liufs@fafu.edu.cn
* Correspondence: ligc@cma.cn

Abstract

Forest carbon and water trade-offs describe the coupling between carbon gain and water availability and are central to predicting forest carbon dynamics under hydroclimate change. Whether and how canopy structural complexity modulates their magnitude and direction, however, remains unclear. Using 7,785,776 high-quality footprints from the Global Ecosystem Dynamics Investigation (GEDI) spaceborne lidar over stable forest pixels across mainland China, we quantified the marginal response of net primary productivity (NPP) to water availability and its moderation by the Waveform Structural Complexity Index (WSCI). A spline-based regression model with tensor-product interactions explained 81.7% of the variance in NPP, and the P−ET × WSCI interaction was highly significant ($F = 92.0$, $p < 0.001$), indicating that the slope of the NPP–water relationship becomes progressively less negative, and eventually positive, as canopy structural complexity increases. The marginal water sensitivity of NPP shifted from negative to positive as structural complexity increased (−19.2, −9.2, and +8.2 g C m^{-2} yr^{-1} per standardized unit in low-, mid-, and high-WSCI forests). Residual carbon–water correlation remained near zero overall ($\rho = 0.0002$) and across WSCI terciles, indicating that structural complexity reshapes the mean water response rather than unexplained coupling. The results were robust across 1–5 km resolutions and to an alternative carbon indicator (aboveground biomass). Structurally complex canopies thus strengthen water-to-carbon conversion efficiency, informing climate-smart forest management.

Keywords: canopy structural complexity; net primary productivity; water availability; waveform structural complexity index

Academic Editor: Vladimír Šebeň

Received: 12 October 2026
Revised: 11 November 2026
Accepted: 21 November 2026
Published: 24 November 2026

Copyright: © 2026 by the authors. Licensee MDPI, Basel, Switzerland. This article is an open access article distributed under the terms and conditions of the Creative Commons Attribution (CC BY) license.

1. Introduction

Forests dominate the terrestrial carbon sink and are central to climate-change mitigation. In China, large-scale afforestation and forest conservation have contributed disproportionately to the global land carbon sink, yet the stability of this sink under accelerating hydroclimatic variability remains uncertain [1]. At the heart of this uncertainty lies the carbon–water trade-off: net primary productivity (NPP) depends on water availability, but water is simultaneously lost through evaporation and transpiration, meaning that carbon gain and

water balance are tightly coupled [2]. Understanding what controls the strength and direction of this coupling is therefore essential for predicting forest carbon dynamics under drought and extreme precipitation. Canopy structural complexity regulates the within-stand allocation of light and water and shapes forest productivity, and therefore serves as a critical factor in forest ecosystem research [3,4]. Revealing the relationships among forest canopy structural complexity, forest productivity, and water availability is essential. It helps predict how forest ecosystems respond to global climate change and supports the development of management strategies for forest conservation and restoration [5–7].

The coupling embodied by these relationships has been extensively investigated across scales and biomes. As carbon assimilation and transpirational water loss share the stomatal pathway, the two fluxes are tightly coupled, and their balance is commonly quantified as water-use efficiency [8]. Water use efficiency describes carbon–water exchange at the leaf-to-canopy scale, and it is not estimated in this study. Instead, we quantify the marginal sensitivity of NPP to climatic water balance, $\partial NPP/\partial(P-ET)$, which represents the change in NPP per unit change in water availability. These two metrics are related but not equivalent: $\partial NPP/\partial(P-ET)$ additionally captures the effects of radiation, nutrients, stand age and canopy structure on carbon uptake, and it is normalized by available water rather than transpired water. Analyses of vegetation greening show that gains in gross and net primary productivity have been accompanied by enhanced evapotranspiration and declining soil water storage, meaning that carbon sequestration is achieved partly at the expense of water availability [9], and satellite records indicate that global greening has driven significant soil moisture loss over more than a third of vegetated land [10]. Earth-system experiments show that soil moisture–atmosphere interactions generate widespread carbon–water trade-offs that intensify under warming and drying [11], while restoration-driven carbon gains carry substantial water costs globally [12]. Plant water stress has also increased widely but remains obscured in water-balance metrics, and greening can decouple terrestrial carbon and water cycles through contrasting effects on water availability. The trade-off is therefore widespread, yet its strength and spatial expression vary markedly among regions, climates, and vegetation types.

Canopy structure, which emerges from species composition and from the diversity of species and tree sizes within a stand, has been proposed as a key regulator of this trade-off. In subtropical forest restoration, tree species diversity and structural complexity jointly drive the stability of productivity [13]. Globally, canopy structural complexity is positively associated with forest productivity and stability, mediated by biodiversity and resource availability [14]. Structural diversity explains aboveground carbon storage more strongly than species diversity across United States forests, although this depends on forest origin and type [15]. A meta-analysis of planted forests on the Chinese Loess Plateau shows that tree mixtures weaken the soil water–biomass trade-off and shift its relative benefit toward water conservation, especially in dry areas [16]. Nevertheless, existing conclusions remain uncertain and partially contradictory. Relationships among structural complexity, species diversity, and productivity vary in magnitude and even in sign across biomes and spatial scales. Species richness may enhance vegetation carbon sequestration while reducing soil carbon storage [17]. Moreover, the water-related consequences of canopy structure are rarely quantified directly, as most studies examine productivity or carbon stocks rather than the marginal carbon response to water availability. Whether structural complexity weakens, strengthens, or merely reshuffles the carbon–water trade-off therefore remains unresolved.

Two gaps prevent a direct answer. First, carbon–water coupling has rarely been assessed systematically along gradients of canopy structural complexity using multi-source, wall-to-wall observations, which limits our ability to predict how forest structure reshapes the carbon–water trade-off. Second, canopy structural complexity remains difficult to

quantify over large domains: complex, multi-layered canopies with high leaf-area and rooting diversity are widely thought to buffer understory microclimate, redistribute soil water, and partition resources across strata, potentially decoupling carbon uptake from short-term water supply, yet most existing metrics are plot-based and therefore not transferable to national-scale analysis. The recent availability of spaceborne lidar from the Global Ecosystem Dynamics Investigation (GEDI) now permits wall-to-wall mapping of canopy structural complexity across entire forest domains [18–20]. In particular, the Waveform Structural Complexity Index (WSCI) derived from GEDI Level 4C data quantified the three-dimensional complexity of forest canopies by incorporating both horizontal and vertical structural components, and thus provides a more comprehensive measure than vertical-only metrics such as Foliage Height Diversity (FHD) [21]. Here, canopy structural complexity is used in the specific sense of the WSCI, a composite, footprint-level index of three-dimensional canopy structure derived from the vertical distribution of lidar returns and calibrated against airborne-laser-scanning measurements of 3D structural complexity. It therefore describes how canopy material is arranged vertically—the number and depth of canopy layers and the vertical foliage profile—rather than the horizontal arrangement of canopy gaps, and it is not assembled from separable horizontal and vertical sub-indices.

In this study, we test whether canopy structural complexity modulates the carbon–water trade-off in China's forests. We hypothesize that the marginal sensitivity of NPP to water availability changes systematically with WSCI, implying that structurally complex forests differ fundamentally in how they couple carbon gain to water supply. Using high-quality GEDI footprints, forest net primary productivity data, climatic data, and two complementary analyses (a spline-based regression model and a residual correlation analysis), we pursued two objectives: (i) to quantify the marginal NPP response to water availability and the moderating effect of the WSCI, and (ii) to test whether the residual correlation between NPP and water availability varies across WSCI terciles. This research characterizes how canopy structural complexity shapes carbon–water coupling.

2. Materials and Methods

2.1. Study Area

The study domain covers forested grid cells across mainland China. These cells were delineated using a stable-forest mask and limited to continuous forests to exclude fragmented agroforest mosaics. We identify pixels with unchanged forest land cover between 2000 and 2025 for subsequent analysis. To reduce biases from land cover classification errors, a pixel was included if it maintained forest cover for at least 23 of the 26 years between 2000 and 2025, that is, if it had no more than three non-forest years, provided that those years were discontinuous. Pixels with more than three non-forest years, or with three consecutive non-forest years, were discarded (Figure 1).

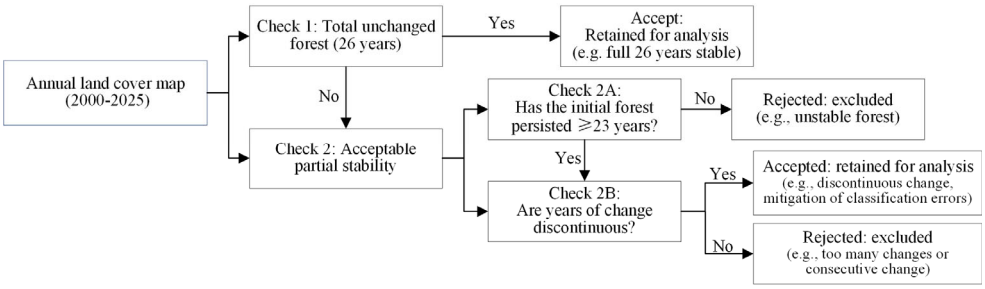


Figure 1. Workflow for identifying stable forest pixels. Annual land-cover maps for 2000–2025 are screened in two steps: pixels whose class never changes are retained (Check 1); pixels that change

are retained only if forest cover persists for at least 23 of the 26 years and the non-forest years are discontinuous (Check 2). Pixels failing either check are excluded.

2.2. Data

The GEDI instrument collects 25m footprint waveform data along orbital transects. Structure diversity metrics, including the Waveform Structural Complexity Index (WSCI), are obtained from the GEDI level 4C (L4C) product and are used here to identify structural diversity hotspots [21]. The WSCI is a waveform-based metric designed to summarize 3D structural complexity at the GEDI-footprint scale using information contained in GEDI relative-height (RH) metrics. In this study, canopy structural complexity refers specifically to the WSCI. The WSCI is established by modeling the relationship between GEDI relative-height (RH) metrics and high-resolution three-dimensional structural complexity derived from airborne laser scanning (ALS) point clouds [22]. As a composite, footprint-level index, the WSCI is not assembled from separable horizontal and vertical sub-indices. WSCI is predicted rather than measured: for each plant functional type, a gradient-boosted model maps GEDI relative-height metrics (RH0–RH100) and foliage cover to ALS-derived 3D structural complexity. Distinct stacked strata produced a broad, multimodal relative-height profile and increased the WSCI value; by contrast, gaps reduce intercepted energy, compress the profile, and decrease the index. As a scalar metric, WSCI integrates the effects of canopy layering and gap information, and it does not provide layer counts or gap-size distributions.

To ensure high-quality data, multiple filters were applied to the GEDI shots.

(1) Only spots for which both the WSCI quality flag (wsci_qf) and the Level 2B quality flag (l2_qf) are set to 1 were retained. The wsci_qf imposes stricter criteria on top of l2_qf: it masks out water and urban areas, applies a higher sensitivity threshold and a denser canopy transmittance requirement, and retains only footprints classified as "tree cover" in ESA WorldCover v200. In other words, observations with wsci_qf = 0 fall outside the WSCI model's training domain rather than representing poor-quality measurements from detection failure. These locations are most likely sparse/degraded forests, forest edges, or sites with insufficient sensitivity caused by overly dense canopies.

(2) A minimum sensitivity threshold of 0.98 was applied [23]. The sensitivity reflects the maximum canopy cover penetration achievable under the signal-to-noise ratio of the waveform and thus represents the ability to detect the ground. Earlier studies have used thresholds of 0.95 or 0.97 [24], and a lower threshold retains more footprints. A threshold of 0.98 was selected to ensure data quality.

(3) The GEDI provides measurements from eight beams, consisting of full-power beams and coverage beams. We excluded coverage beams and only adopted full-power beams in our analysis.

In summary, we identified WSCI footprints within pixels where forest type remained unchanged over the past two decades and included them in the analysis. We calculated the footprint-mean WSCI by aggregating the WSCI to a 1 km grid, excluding grids with fewer than five footprints due to low confidence. No interpolation or modeling was performed to generate this gridded dataset, meaning that only grid cells where high-quality GEDI footprints were observed are represented.

Carbon flux and water-balance variables were drawn from remote-sensing products to avoid spurious covariance between reanalysis drivers and responses: NPP and Evapotranspiration (ET) from GLASS (Global Land Surface Satellite Products); precipitation (P) from China Meteorological Forcing Data (CMFD) [25]. We calculated the annual water availability (WA) at each grid cell by subtracting the annual actual evapotranspiration from the annual precipitation [26,27].

Aboveground biomass (AGB) was used in robustness checks. The AGB dataset was produced by integrating multi-source remote sensing data with deep learning approaches, including residual neural networks [28]. SRTM data were used to generate the Digital Elevation Model (DEM) and to derive slope and aspect across the study area. Temperature, downward shortwave radiation (Srad), and Relative humidity (Rhum) were extracted from the CMFD 2.0 dataset. Soil moisture, Palmer Drought Severity Index (PDSI), and Vapor Pressure Deficit (VPD) were obtained from TerraClimate. Descriptive statistics for the variables used in the analysis are summarized in Table S1.

All spatial layers were harmonized to a China Albers equal-area projection (central meridian 105° E, standard parallels 25° N and 47° N; units: meters), which preserves constant grid-cell area across latitudes and avoids distance distortion in spatial smoothing and blocked cross-validation. The final analytical sample comprised 338,598 forested 1 km grid cells. Finer layers (NPP) were aggregated by mean; coarser layers (P, climate) were resampled to 1 km by using bilinear interpolation. DEM and GEDI WSCI (Waveform Structural Complexity Index) footprints, stored in WGS84 geographic coordinates, were reprojected to China Albers before gridding. A stable-forest mask restricted the analysis population; grid cells missing any key variable were excluded.

The GEDI collected data from 4 April 2019 to 16 March 2023, when the instrument was moved to an alternate location on the ISS; data collection resumed only on 26 April 2024. Within that window, the years are not equivalent: 2019 begins on 4 April and 2023 ends on 16 March, so both are truncated. Of the complete years, 2022 provides the largest single-year footprint archive over China. The GEDI L4C footprints used here are those acquired during the 2022 GEDI mission year, merged into a single national footprint set; the WSCI therefore describes the canopy structure sampled by the GEDI in that year. All biophysical and climatic covariates correspond to the year 2022 to maintain consistency with the GEDI observations. Temporal alignment of all variables was implemented in three sequential steps: products with the same nominal year were selected, all layers were harmonized to a consistent 1 km Albers projection grid for China, and only grid cells with valid values were retained across all layers. No temporal interpolation, smoothing or lagging was applied.

2.3. Statistical Analyses

We adopted two complementary analyses. First, a spline-based regression model characterizes how the WSCI moderates the NPP and water relationship. Second, a residual correlation analysis quantifies the post-covariate correlation between NPP and water availability after accounting for covariates. This correlation directly represents the carbon and water trade-off. The analysis further captures how this trade-off varies with structural complexity.

2.3.1. Spline-Based Regression Model of the NPP–Water Response

Continuous predictors were z-score-standardized ($x^* = (x - \mu)/\sigma$, with μ and σ estimated over forest grid cells) to improve coefficient comparability and model stability. The NPP response was retained in original units, whereas water availability (P−ET) was standardized as z_{WA}. Climate–soil–topographic covariates (evapotranspiration, precipitation, temperature, solar radiation, relative humidity, VPD, PDSI, soil moisture, and elevation; nine variables) exhibited substantial multicollinearity (initial Variance Inflation Factor (VIF) > 5 for several). We reduced this block using principal component analysis (PCA) and retained the first four principal-component axes (PC1–PC4), which together explained 93.5% of the variance (PC1 44.3%, PC2 23.5%, PC3 17.7%, PC4 8.0%), entering them as linear climate–environment axes that jointly control for temperature, radiation, and drought confounding. Elevation was included as a separate smooth term (cr(dem, *df*

= 6)) rather than in the PCA block. The spatial distributions of PC1–PC4 scores, elevation, and the principal climate variables are shown in Figure S1.

To disentangle the independent and interactive nonlinear effects of the precipitation–evapotranspiration balance (P−ET) and the WSCI on forest NPP, while accounting for climatic covariates, topographic variation, and large-scale spatial autocorrelation across forest grid cells, we fitted a spline-based regression model using ordinary least squares. Natural cubic splines were used to capture nonlinear marginal effects, and the core interaction between water availability and the WSCI was specified as a tensor-product interaction of the two univariate spline bases. For each forest grid cell i, the model was specified as:

$$\begin{aligned} NPP = \beta_0 + f_{P-ET}(z_{P-ET}) + f_{wsci}(z_{wsci}) + f_{interaction}(z_{P-ET}, z_{wsci}) \\ + f_{clim}(PC1, PC2, PC3, PC4) + f_{dem}(z_{dem}) + f_{space}(x, y) + \varepsilon \end{aligned} \quad (1)$$

In Equation (1), β_0 denotes the model intercept; $f_{P-ET}()$ and $f_{wsci}()$ represent the natural-cubic-spline main-effect terms for standardized P−ET and the standardized WSCI, respectively. Each univariate spline was constructed on a set of fixed interior knots, with the basis dimension (degrees of freedom) specified a priori. Appendix A expands the model term by term.

The core nonlinear interaction between z_{P-ET} and z_{wsci} was specified as the tensor product of the two univariate spline bases, which parameterizes the interactive surface without refitting marginal main effects that are already incorporated in $f_{P-ET}()$ and $f_{wsci}()$.

In Equation (1), k does not appear as a regression coefficient but denotes the basis dimension or the effective degrees of freedom—of each univariate natural-cubic-spline basis from which the smooth terms $f_{P-ET}()$, $f_{wsci}()$, $f_{dem}()$, and $f_{space}()$ are constructed. In compact notation, each $f()$ in Equation (1) represents a linear combination of k natural-cubic-spline basis functions evaluated at its covariate, so k determines the number of coefficients fitted for that term and, in turn, the maximum curvature it can represent. Because k is a pre-specified model hyper-parameter rather than an estimated regression coefficient, it is not written explicitly in the formula. The interaction term $f_{interaction}(z_{P-ET}, z_{wsci})$ is the tensor product of the two univariate spline bases, whose dimension is $k_{P-ET} \times k_{wsci}$. We set $k = 8$ for the P−ET and WSCI splines (so the tensor-product interaction comprises 8 × 8 = 64 basis functions), $k = 6$ for the elevation spline, and $k = 12$ for each of the two spatial splines. These values were fixed before fitting, following the usual rule of thumb that a natural cubic spline basis with k functions can represent up to about $k - 2$ direction changes while leaving enough residual degrees of freedom for inference. A sensitivity analysis over k = 5, 6, 8, 10 and 12 showed that the interaction remained significant and that the sign reversal across terciles persisted at every value tested, with the tercile slopes changing by no more than ±2 g C m^{-2} $yr^{-1}$and the interaction F-statistic ranging from 42.8 to 247.5.

The terms *PC1–PC4* denote the first four principal-component axes derived from climate–environment PCA, entered as linear predictors to mitigate multicollinearity among raw climatic variables. $f_{dem}()$ is the natural cubic-spline term for standardized elevation (z_{dem}), accounting for topographic effects on NPP. The spatial terms $f_{space}(x)$ and $f_{space}(y)$ are univariate natural-cubic-spline terms fitted on the Albers equal-area coordinates ($k = 12$ each), which absorb large-scale residual spatial structure originating from gridded geographic data and alleviate biased significance inference. The residual term ε captures unexplained stochastic variation. The model was estimated by OLS. Approximate F-tests were applied to evaluate the statistical significance of the tensor-product interaction term. The magnitude of forest structural complexity effects was quantified by computing first-order partial derivatives $\partial NPP/\partial(P-ET)$ across the observed gradient of the WSCI, obtained from finite differences in the fitted response surface.

To further characterize how water conditions modulate these sensitivities, forest grid cells were cross-classified into WSCI terciles (lower, middle, and upper third of the WSCI

distribution) and water-availability strata defined on the standardized water balance (z_{P-ET}): dry (below the 35th percentile, i.e., P−ET < −228.58 mm yr^{-1}), mid (35th–65th percentiles, −228.58 ≤ P−ET ≤ 52.25 mm yr^{-1}), and wet (above the 65th percentile, P−ET > 52.25 mm yr^{-1}); the 5th–95th percentile window was used to trim extreme water-balance outliers. Negative partial-derivative slopes indicate NPP declining as water availability increases (water-non-limiting, largely light- or temperature-controlled conditions), whereas positive slopes indicate enhanced carbon uptake with increasing water availability (water-responsive conditions); the shape of the interaction surface characterizes how this slope varies along the WSCI gradient.

2.3.2. Residual Carbon–Water Correlation and Its Uncertainty

To quantify the carbon–water trade-off after removing confounding effects of climate, topography, and spatial structure, we computed the Pearson correlation coefficient ρ between the residuals of the regression model in Section 2.3.1 for NPP and for standardized P−ET. This residual correlation captures whether, after controlling for covariates, forests that are more productive than expected also tend to experience higher-than-expected water availability (positive ρ, synergistic residual patterns) or the opposite (negative ϱ, decoupled residual patterns).

To compute each residual series, we fitted the regression model in Section 2.3.1 once with NPP as the response and once with standardized WA as the response, retaining the residuals of both fits. The two fits differ in their right-hand side. In the first fit, NPP is the response and the predictors are $f(z_{P-ET})$, $f(z_{WSCI})$, their tensor-product interaction, PC1–PC4, $f(z_{DEM})$ and the two spatial splines (Equation (1)). In the second fit, standardized water availability (z_{WA}) is the response and the predictors are PC1–PC4, $f(z_{DEM})$ and the two spatial splines only; the z_{P-ET} main effect and the P−ET × WSCI interaction are removed from the right-hand side, because z_{WA} cannot appear on both sides of the same equation. The residual of the first fit therefore represents NPP variation that remains after climate, topography, space, and water availability itself have been accounted for, whereas the residual of the second fit represents WA variation that remains after climate, topography and space have been accounted for. Because both fits use the same covariate block and the same spline bases, the two residual series are controlled for a common environmental structure, and ρ is the Pearson correlation between them.

Because the residuals are non-independent by construction, uncertainty in each ρ estimate and in $\Delta\rho$ was quantified by a spatially blocked bootstrap. Blocks were the 100 km × 100 km tiles defined on the Albers equal-area coordinates that were also used for blocked cross-validation (Section 2.3.3). In each of 3000 iterations, tiles were resampled with replacement, both models were refitted on the selected tiles, the residuals were recomputed, and ρ was recalculated; 90% confidence intervals were taken as the 5th and 95th percentiles of the bootstrap distribution. Blocking ensures that observations carried into a resample are separated by distances larger than the range of the residual spatial autocorrelation detected by Moran's I test (I = 0.160, p = 0.005).

To characterize how structural complexity modulates this trade-off, forecast grids were stratified into three groups according to WSCI terciles, representing low, moderate, and high forest structural complexity. The residual correlation was estimated separately within each stratum, yielding stratum-specific estimates $\rho(low)$, $\rho(mid)$, and $\rho(high)$. We defined the key contrast metric as follows:

$$\Delta\rho = \widehat{\rho}(high) - \widehat{\rho}(low) \quad (2)$$

A non-zero $\Delta\rho$ whose 90% confidence interval excludes zero indicates that forest structural complexity significantly modulates the magnitude of carbon–water trade-offs. Ecological interpretation of residual correlation ρ follows: a negative ρ indicates

decoupled residual fluctuations, whereas a positive ρ denotes co-varying (synergistic) residual patterns.

2.3.3. Validation and Diagnostics

Model performance and inferential quality were assessed via (i) the in-sample R^2 of the regression model in Section 2.3.1, together with an approximate F-test of the tensor-product interaction term; (ii) a permutation-based Moran's I test applied to the model residuals to detect residual spatial autocorrelation. Uncertainty in the residual correlation estimates was quantified by the bootstrap procedure.

We also performed a spatial resolution sensitivity test. The primary analysis was carried out at 1 km and repeated at 0.5, 2 and 5 km. We compared the direction and magnitude of the WSCI moderation effect (the tensor-product interaction between P−ET and WSCI) across these grids. These comparisons confirmed the stability of our qualitative conclusion across different resolutions. Furthermore, we used AGB as an alternative to NPP to test whether the WSCI-mediated moderation of the carbon–water response depends on the choice of carbon indicator. We reran the regression analysis substituting aboveground biomass for NPP.

3. Results

3.1. Canopy Structural Complexity Reverses the NPP–Water Sensitivity from Negative to Positive

After quality filtering, the final GEDI dataset contained 7,785,776 high-quality WSCI footprints from stable forest pixels (Figure 2). These footprints covered 338,598 forested 1 km grid cells across China's forest. Mean annual NPP was 798.6 ± 174.2 g C m^{-2} yr^{-1}, and mean water availability (P−ET) was 352.8 ± 456.3 mm yr^{-1}, with large geographic variation. The regression model, specified with natural cubic splines and a tensor-product interaction between water availability and the WSCI, explained 81.7% of the variance in NPP (R^2 = 0.817).

Figure 3 was produced from the spline-based regression model, which was fitted to observed NPP (g C m^{-2} yr^{-1}) as the response variable using natural cubic splines with a tensor-product interaction between standardized water availability (P−ET) and canopy structural complexity, while controlling for topography, climate principal components, and spatial location. Figure 3a shows the predicted NPP–water response curves for the low-, mid-, and high-WSCI terciles, with all covariates held at their sample means. The divergence in curve shape reflects an ecological mechanism whereby structurally complex canopies buffer microclimate, redistribute water through deeper rooting, and stratify resource acquisition, increasing water-use efficiency so that high-WSCI forests gain the most carbon per unit of additional water. Figure 3b reports the residual correlation ϱ(NPP, P−ET) by WSCI tercile with bootstrap 90% confidence intervals, testing whether structural complexity alters the coupling of unexplained carbon–water fluctuations; values near zero indicate that no residual regime shift accompanies the WSCI gradient. Figure 3c presents marginal water sensitivity $\partial NPP/\partial(P-ET)$ grouped by WSCI tercile. This metric describes the predicted change in NPP per one-standard-deviation rise in water availability. It therefore measures the marginal sensitivity of carbon uptake to water supply rather than water-use efficiency: a positive value indicates that additional available water is associated with higher NPP, while a negative value indicates the opposite. Specifically, sensitivity changes from negative to positive as structural complexity increases. The partial slope of NPP with respect to standardized water availability shifted from negative to positive with increasing structural complexity: −19.2 g C m^{-2} yr^{-1} per standardized unit in low-WSCI forests, −9.2 in mid-WSCI forests, and +8.2 in high-WSCI forests. Thus, the marginal

sensitivity of NPP to water availability was reversed in sign rather than simply weakened by canopy structural complexity.

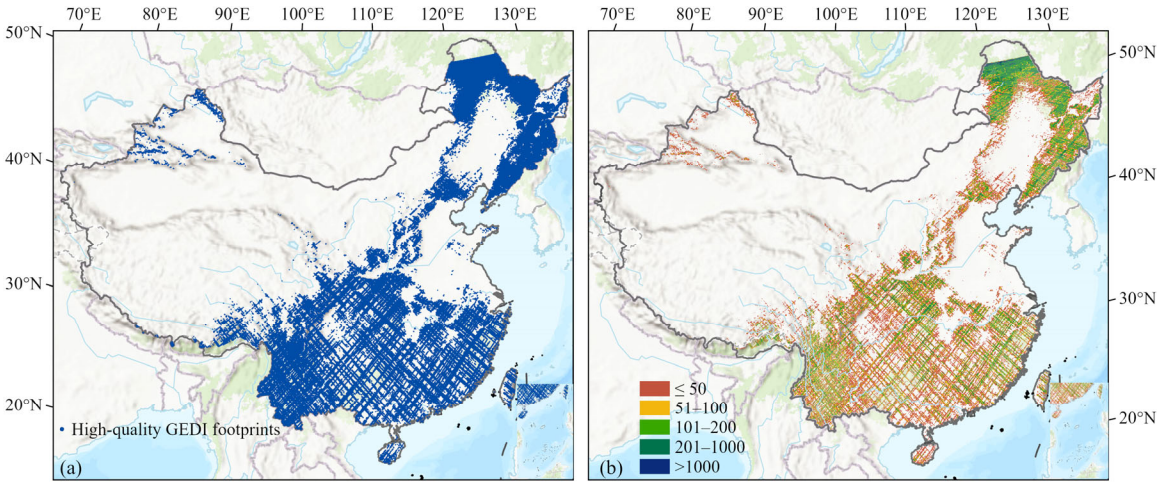


Figure 2. Spatial distribution of (**a**) the high-quality GEDI footprints used for WSCI derivation and (**b**) GEDI footprint density (footprints km^{-2}).

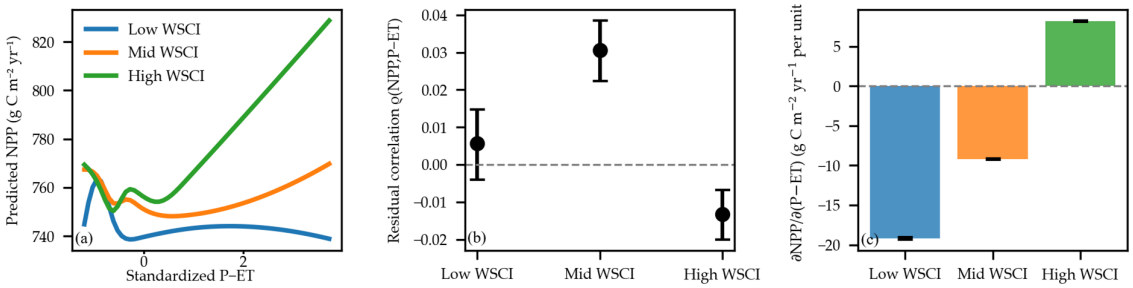


Figure 3. Canopy structural complexity modulates the NPP–water relationship in Chinese forests. (**a**) Predicted NPP as a function of standardized water availability (P−ET) for the low-, mid-, and high-WSCI terciles. (**b**) Residual correlation ρ(NPP, P−ET) with bootstrap 90% confidence intervals for each WSCI tercile; the dotted line marks $\rho = 0$. (**c**) Marginal water sensitivity ∂NPP/∂(P−ET) (±SE) by WSCI tercile, showing a shift from negative to positive sensitivity as WSCI increases.

3.2. WSCI Weakens the NPP Response to Water Availability

Both water availability (P−ET) and canopy structural complexity were strong predictors of NPP (both $p < 0.001$). Crucially, the tensor-product interaction between P−ET and the WSCI was highly significant ($F = 92.0$, $p < 0.001$), indicating that the slope of the NPP–water relationship changes systematically along the WSCI gradient (Figure 4). To examine how water conditions moderate this response, grid cells were stratified into WSCI terciles (lower, middle, and upper third of the WSCI distribution) and water-availability strata defined on the 35th and 65th percentiles of standardized P−ET (dry, mid, and wet). When stratified by WSCI terciles, high WSCI forests showed the strongest positive water sensitivity under wet conditions (∂NPP/∂(P−ET) = +17.8 g C m^{-2} yr^{-1} per standardized unit in the wet P−ET stratum), whereas low-WSCI forests exhibited strongly negative sensitivity under dry conditions (−26.1).

This cross-stratification reveals a consistent sign reversal in the marginal water sensitivity of NPP along the water-availability gradient, which can be understood mechanistically through the changing role of water balance across strata. In the dry stratum (P−ET < −228.58 mm yr^{-1}), where evapotranspiration exceeds precipitation and forests experience a large net water deficit, water and energy (temperature and radiation) are negatively

coupled in space; grid cells with slightly higher P−ET tend to be associated with stronger evaporative demand and greater thermal stress. A marginal increase in water availability within this stratum is therefore not equivalent to a release of water limitation; the additional water is rapidly consumed by high evaporative demand and is accompanied by stomatal regulation and elevated maintenance respiration, so water-use efficiency is low, and carbon assimilation tends to decline—hence, the negative partial derivative. In the wet stratum (P−ET > 52.25 mm yr^{-1}), where precipitation exceeds evapotranspiration and water is no longer the primary limiting factor, a marginal increase in P−ET represents a genuine increase in water surplus under well-watered, water–energy-synchronous conditions, directly promoting stomatal opening and photosynthesis and therefore yielding a positive marginal sensitivity. The mid stratum (−228.58 ≤ P−ET ≤ 52.25 mm yr^{-1}) is a transition in which water limitation is progressively alleviated and the water–energy coupling shifts from negative toward neutral, with partial derivatives converging toward zero (−13.6 to −3.5). Importantly, the WSCI moderation operates primarily at the wet end: high-WSCI forests exhibited the strongest positive sensitivity (+17.8), indicating that structurally complex canopies most efficiently convert additional water into carbon when water is not limiting, whereas even structurally complex forests could not reverse the negative response under severe water deficit (−21.9 to −26.1). The reversal of ∂NPP/∂(P−ET) from negative under dry conditions to positive under wet conditions is thus a consistent, mechanistic consequence of how water balance mediates water–energy coupling and water-use efficiency along the productivity gradient, and it is preserved across WSCI terciles (Figure 4).

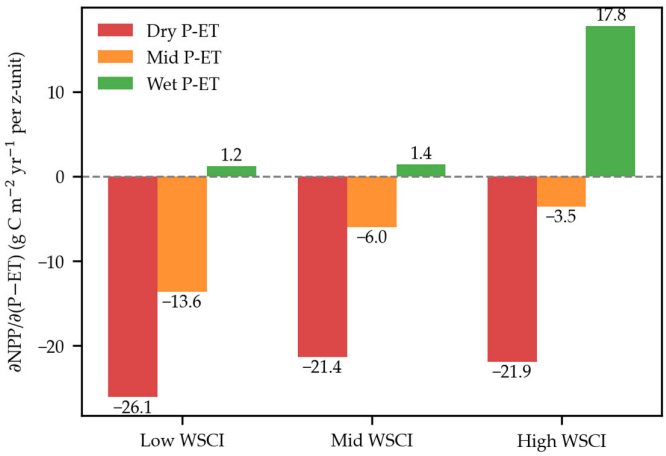


Figure 4. Marginal water sensitivity ∂NPP/∂(P−ET) across WSCI terciles and water-availability strata. Strata are defined on standardized P−ET as dry (below the 35th percentile, P−ET < −228.58 mm yr^{-1}), mid (35th–65th percentile, −228.58 ≤ P−ET ≤ 52.25 mm yr^{-1}) and wet (above the 65th percentile, P−ET > 52.25 mm yr^{-1}).

The continuous, two-dimensional structure of the marginal water sensitivity is shown in Figure 5, which complements the discrete tercile cross-stratification of Figure 4. The heat map, evaluated from the regression surface of Section 2.3.1 over the joint gradient of standardized WSCI and P−ET (with all other covariates held at their sample means), is dominantly negative across the dry part of the gradient, reaching about −40 g C m^{-2} yr^{-1} per standardized unit under severe deficit (P−ET below −350 mm yr^{-1}), and becomes positive in the wet part, exceeding +20 where P−ET is positive and WSCI lies in the upper tercile. The positive sensitivity is most pronounced at the wet end and increases with WSCI, reaching its maximum (≈+25) in high-WSCI forests under wet conditions—consistent with the tercile-level result that structurally complex canopies most efficiently

convert additional water into carbon when water is not limiting. The transition is not uniform along the WSCI axis: within the dry stratum the sensitivity weakens as the deficit decreases and locally changes sign in narrow bands close to the dry/mid boundary, most clearly for mid- and high-WSCI forests. These bands occupy a small part of the dry stratum and do not affect the tercile means, which remain negative for all three WSCI terciles in the dry stratum (−26.1, −21.4 and −21.9; Figure 4). The strongest positive sensitivities are therefore found where water is not limiting and structural complexity is high, which is also where the tercile analysis places its largest positive value (+17.8). Thus, the sign reversal of the marginal water sensitivity is a continuous, structurally modulated transition rather than a discrete threshold between water strata.

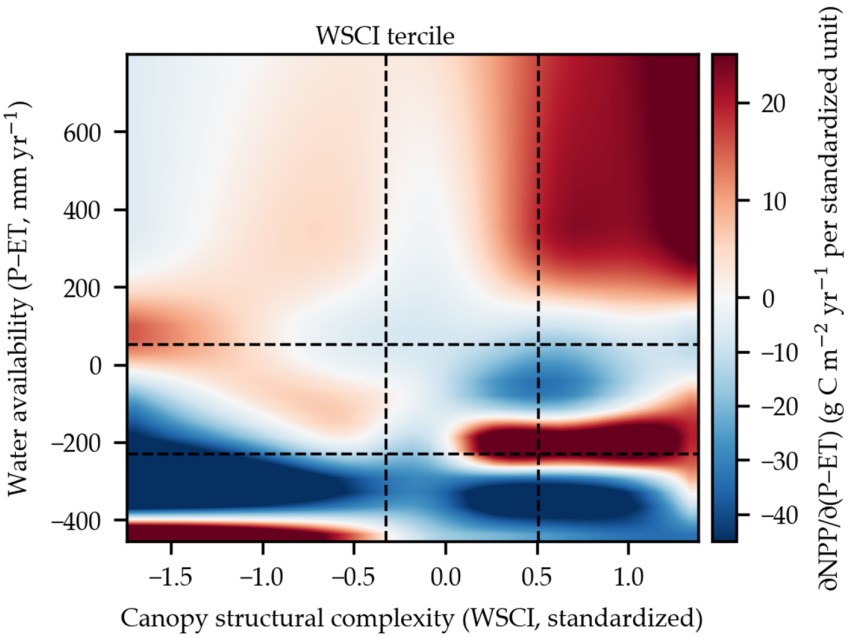


Figure 5. Continuous variation in marginal water sensitivity with WSCI and P−ET. Colors give ∂NPP/∂(P−ET) evaluated on the fitted surface with all other covariates at their sample means. Dashed vertical lines mark the WSCI tercile boundaries; dashed horizontal lines mark the water-availability stratum boundaries (P−ET = −228.58 and +52.25 mm yr^{-1}). The surface is shown over the 5th–95th percentile range of both covariates.

3.3. Residual Carbon–Water Coupling by Structural Complexity

The residual correlation ρ between NPP and P−ET was estimated after accounting for climate, topography, and spatial location, using block bootstrap to obtain 90% confidence intervals. Across all 338,598 grid cells, the residual correlation was essentially zero (ρ = 0.0002; 90% CI: −0.0046, 0.0049; Table 1). The near-zero residual coupling confirms that the model's mean climatic, topographic, and spatial terms fully captured covariation driven by environmental gradients. No systematic residual carbon–water trade-off remains at the national scale. Accordingly, the WSCI-mediated shift in NPP–water sensitivity reported in Section 3.2 reflects a real change in the marginal water response of carbon uptake. This pattern is not an artifact of unmodeled confounding factors. Furthermore, canopy structural complexity regulates the carbon–water relationship via the mean sensitivity response instead of unexplained residual coupling.

Table 1. Diagnostics for the spline-based regression model and the residual correlation analysis.

Diagnostic	Value	Criterion/Interpretation
In-sample R^2 of the spline regression model	0.817	Variance in NPP explained by the regression model; higher is better.
Tensor-product interaction (F-test)	F = 92.0, $p < 0.001$	Highly significant; the WSCI moderation effect is not attributable to chance.
Residual spatial autocorrelation (Moran's I)	0.160 ($p = 0.005$)	Significant at $\alpha = 0.05$; mild residual spatial structure.
Overall residual correlation ρ (NPP, P−ET)	0.0002 (90% CI: −0.0046, 0.0049)	Near zero; no systematic residual carbon–water coupling at the national scale.
Tercile residual correlations ρ (low/mid/high)	0.006/0.031/−0.013	90% confidence intervals in Section 3.3; no sign reversal across WSCI terciles.

The 90% confidence intervals for the residual correlations were obtained by nonparametric block bootstrap (3000 resamples, seed 42). The tensor-product interaction was evaluated by an F-test against the no-interaction model; ρ overall denotes the residual Pearson correlation between NPP and P−ET after covariate control.

Stratifying forests by WSCI terciles did not reveal any reversal in the sign of ρ. The residual correlation remained close to zero in all terciles: low-WSCI $\rho = 0.006$ (90% CI: −0.004, 0.015), mid-WSCI $\rho = 0.031$ (90% CI: 0.022, 0.038), and high-WSCI $\rho = -0.013$ (90% CI: −0.020, −0.007). Although the mid-WSCI tercile was weakly positive and statistically distinguishable from zero, the magnitudes were small and provided no evidence for a regime shift from water-tracked to water-buffered carbon dynamics.

3.4. Model Diagnostics

Model uncertainty was quantified by block bootstrap (3000 resamples per estimate); the 90% confidence intervals for the residual correlation were narrow, confirming precise estimation at the sample size used (n = 338,598). The tensor-product interaction remained highly significant across terciles, supporting the robustness of the WSCI moderation effect. Cross-validation and residual spatial-autocorrelation diagnostics are summarized in Table 1.

3.5. Robustness of the WSCI Moderation Effect Across Grid Resolutions

To assess whether the WSCI-mediated moderation of the NPP–water response depends on grid resolution, we repeated the primary 1 km analysis at 0.5 km, 2 km, and 5 km. The model explained a similar share of NPP variance at all resolutions (R^2 = 0.831, 0.817, 0.813, and 0.812 at 0.5, 1, 2, and 5 km), and the tensor-product interaction remained highly significant in every case (F = 122.8, 92.0, 48.9, and 17.0; all $p < 0.001$). The marginal sensitivity of NPP to water availability increased monotonically with WSCI at each resolution, shifting from negative to positive across WSCI terciles: from −19.2 to +8.2 g C m^{-2} yr^{-1} per standardized unit at 1 km, from −17.8 to +10.5 at 2 km, and from −7.8 to +15.96 at 5 km (Table 2). Absolute partial derivatives varied across resolutions. This reflects that grid aggregation reshapes sampled water-balance and productivity gradients. Even so, the qualitative pattern of WSCI moderation was consistent across all four resolutions (Figure 6). The sign shifted from water-suppressed to water-responsive carbon uptake with rising structural complexity. The residual carbon–water correlation also remained effectively zero at every resolution (ρ = 0.000–0.0002; all 90% CIs spanned zero).

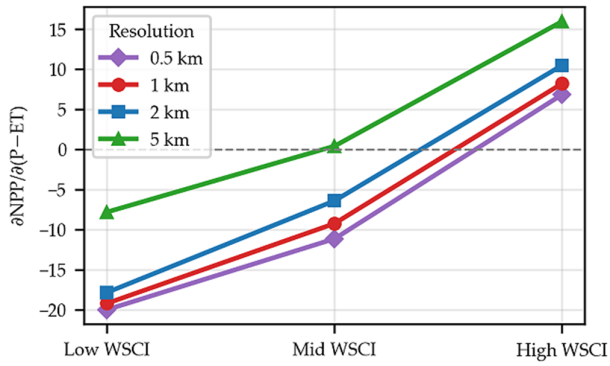


Figure 6. Marginal water sensitivity ∂NPP/∂(P−ET) across WSCI terciles at different grid resolutions.

Table 2. Estimates for the robustness of the WSCI moderation effect across grid resolutions.

Resolution	*n*	R^2	Interaction F	dNPP/d(P−ET) Low	dNPP/d(P−ET) Mid	dNPP/d(P−ET) High	Residual ρ (90% CI)
0.5 km	532,678	0.831	122.8	−20.00	−11.15	+6.84	0.000 (−0.004, 0.004)
1 km	338,598	0.817	92.0	−19.2	−9.2	+8.2	0.000 (−0.005, 0.005)
2 km	146,544	0.813	48.9	−17.8	−6.4	+10.5	0.000 (−0.007, 0.007)
5 km	39,329	0.812	17.0	−7.8	+0.4	+16.0	0.000 (−0.013, 0.013)

n, number of forest grid cells; F, approximate F-statistic of the tensor-product interaction (all $p < 0.001$); ∂NPP/∂(P−ET), marginal sensitivity in g C m^{-2} yr^{-1} per standardized unit by WSCI tercile; ρ, residual NPP–P−ET correlation with bootstrap 90% confidence interval.

3.6. Robustness of the WSCI Moderation Effect to an Alternative Carbon Indicator (Aboveground Biomass)

To test whether the WSCI-mediated moderation of the carbon–water response depends on the specific carbon indicator used, we repeated the regression analysis with aboveground biomass replacing NPP as the carbon indicator, keeping the same model structure and the same AGB-valid subset of forest grid cells (n = 338,582). The model explained 61.4% of the variance in AGB (R^2 = 0.614), and the tensor-product interaction between P−ET and WSCI remained highly significant (F = 33.4, $p < 0.001$). As with NPP, the marginal sensitivity of AGB to water availability shifted from negative to positive with increasing structural complexity, rising monotonically from −6.4 Mg ha^{-1} per standardized unit in low-WSCI forests to +2.9 in mid-WSCI and +7.7 in high-WSCI forests, compared with −19.2/−9.2/+8.2 g C m^{-2} yr^{-1} per standardized unit for NPP on the same subset. The sign reversal and monotonic increase in water sensitivity along the WSCI gradient remained consistent when biomass was used as the carbon metric instead of net primary productivity. This finding indicates that the WSCI-mediated modulation of carbon–water response is robust to the selection of carbon indicators.

4. Discussion

4.1. Structural Complexity and the Marginal Water Response

Canopy structural complexity is already known to raise forest productivity and to make it more stable: complex canopies accumulate more carbon, and their productivity tracks climate more weakly than structurally simple canopies, a pattern reproduced in canopy-resolving simulations, in unevenly aged mixed stands, and in diversity–productivity analyses, where structural diversity outweighs species diversity in regulating spatial variation in productivity and mediates the climate sensitivity of productivity [29]. Our results agree with this body of literature on direction but differ in what is measured:

previous studies have quantified how much carbon a canopy holds, or how strongly its productivity follows climate, but none describes how an additional unit of water becomes carbon. The marginal sensitivity ∂NPP/∂(P−ET) does that, showing that the advantage of complex canopies is a steeper, positive water response rather than a uniformly higher carbon level—the water-axis counterpart of the productivity–complexity relationship established at the carbon axis.

The near-zero residual correlation across all WSCI terciles indicates that, once mean climatic, topographic, and spatial effects are removed, there is little systematic coupling between unexplained NPP and water-availability variation at the national scale, regardless of structural complexity. The primary signal lies in the mean response. Simple, structurally homogeneous canopies with low WSCI exhibit negative marginal water sensitivity. Under water deficit conditions, extra water is mostly lost via evaporation rather than converted into carbon. In contrast, structurally complex canopies with high WSCI show positive marginal water sensitivity. This pattern aligns with the capacity of complex canopies to buffer microclimates, access deeper soil water via diverse root systems, and partition resources across vertical strata. As a result, added water can be converted into proportionally larger carbon gains.

Our results are consistent with a growing body of evidence that structurally complex forests sustain higher and more stable productivity. Globally, increasing canopy structural complexity is associated with higher and more stable ecosystem productivity [14], structural diversity mediates the sensitivity of productivity to climate [30], and compositionally diverse canopies enhance productivity [31]. At stand-to-regional scales, diversity and structure jointly govern the stability of productivity during subtropical forest restoration [32], and structural and species diversity strengthen resistance to drought [33,34]. Our finding that the marginal NPP–water response shifts from negative to positive with increasing structural complexity extends this consensus from the carbon axis to the water axis, and it parallels evidence that tree mixing weakens the soil water–biomass trade-off in planted forests [35]. Our analysis reconciles these views: a carbon–water trade-off is the norm for structurally simple forests, but it is progressively offset as structural complexity increases. Compared with the earlier studies, in this study, rather than comparing static carbon stocks or water-use-efficiency proxies, we estimate the marginal sensitivity ∂NPP/∂(P−ET) directly, thereby isolating the marginal carbon response to water that ultimately governs the trade-off. We separate the mean marginal response from residual carbon–water coupling: the near-zero residual correlation shows that structural complexity acts through the mean sensitivity rather than through unexplained covariation, a decomposition that has rarely been tested and that guards against attributing confounding to structure. The sign reversal is further robust across 0.5–5 km grid resolutions and to an alternative carbon indicator (aboveground biomass), addressing the scale dependence and indicator sensitivity that hamper comparison. These features connect plot-level mechanisms with national-scale patterns of the carbon sink, providing a more transferable basis for water-sensitive forest management than site-specific assessments alone.

4.2. The Dry-to-Wet Sign Reversal and Its Underlying Mechanisms

A first-order observation underlying the WSCI-mediated shift is the sign reversal of marginal water sensitivity along the water-availability gradient itself, which reflects how water balance modulates water–energy coupling and water-use efficiency. This dry-to-wet reversal is the ecological baseline upon which structural complexity acts; it was observed in all WSCI terciles, and structural complexity primarily amplified the positive response at the wet end rather than mitigating the negative response at the dry end, where even structurally complex forests remained negatively sensitive. We therefore interpret the WSCI moderation as an enhancement of the marginal carbon response to water under

water-replete conditions, rather than as an improvement in water-use efficiency, which this analysis does not estimate; it is superimposed on a general, hydro-climatically driven sign reversal of marginal sensitivity.

Several non-exclusive mechanisms can explain why increasing structural complexity shifts the marginal NPP–water response from negative to positive, that is, why it strengthens the conversion of additional water into carbon. (1) Microclimate buffering. Complex canopies generate cooler, more humid understory microclimates that reduce vapor pressure deficit and heat stress on photosynthetic tissues, thereby sustaining carbon uptake during periods of high atmospheric water demand [36]. (2) Hydraulic redistribution and deep rooting. Structurally heterogeneous forests tend to have deeper and more diverse root systems that can access stored soil water and redistribute it vertically, maintaining transpiration and photosynthesis during dry spells [37]. (3) Vertical resource partitioning. Multi-layered canopies distribute light, water, and nutrient use across strata, reducing competition for any single limiting resource and stabilizing whole-canopy carbon uptake [38]. (4) Structural and demographic legacies. Complex stands often contain older, larger trees with greater carbohydrate storage and more conservative water-use strategies, which can decouple current-year NPP from current-year water stress [39]. These mechanisms are not mutually exclusive and most likely act synergistically, meaning that the WSCI moderation is best interpreted as a continuous amplification of the mean marginal water response rather than as a discrete threshold.

Two features of the fitted surface deserve comment. First, the sensitivity is negative in a narrow zone at high WSCI and intermediate P−ET, immediately below the dry/mid boundary. One explanation, which the analysis cannot separate from the others, is that the stands with the highest structural complexity are those with the largest leaf area and the greatest transpirational demand, so that near a neutral water balance a marginal increase in water surplus is consumed by the canopy's own water use before it can be invested in additional carbon; in addition, cells near P−ET ≈ 0 tend to occur where cloud cover is higher and shortwave radiation lower, so that the additional water arrives with less energy to convert it. Second, the transition is abrupt at low WSCI and low P−ET. There, the marginal response is dominated by evaporative demand, which rises steeply as the deficit deepens, and a simple canopy has no buffering capacity to attenuate that rise; the surface therefore changes sign over a short distance in P−ET. Part of the apparent sharpness is also a property of a fitted surface near the ends of the sampled range, which is why Figure 5 displays the surface over the 5th–95th percentile range of both covariates and why we caution against reading the outer bands as sharp ecological thresholds.

4.3. Limitations

Several limitations should be considered when interpreting these findings. First, residual spatial autocorrelation was significant (Moran's $I = 0.160$, $p = 0.005$), indicating unmodeled spatial dependence; future models should replace the spatial spline terms with an explicit spatial correlation structure (e.g., conditional autoregressive or Markov random-field models) to obtain more reliable uncertainty estimates. Second, the mid-WSCI tercile showed a weak but statistically distinguishable positive residual correlation ($\rho = 0.031$, 90% CI: 0.022–0.038), indicating that a small amount of carbon–water covariation remains unexplained even after covariate control; although the magnitude is negligible relative to the marginal sensitivities, it cautions against interpreting the near-zero residual coupling as complete statistical independence. It should be noted that P−ET serves as a climatic water balance proxy reflecting the net atmospheric water supply at the land surface rather than a comprehensive index of hydrological water availability, as it does not explicitly account for runoff generation, groundwater recharge, soil water storage

dynamics, or anthropogenic water withdrawals. Therefore, all statements about water availability here refer to the climatic balance only.

4.4. Implications for Forest Management and Restoration

Forests are a substantial part of the global land carbon sink [40]. Management and restoration policies have favored fast-growing, structurally simple plantations precisely because they maximize carbon sequestration rates [41,42]. Our results suggest that greater canopy structural complexity can improve forest carbon sink resilience under water stress. Such complexity may be achieved via mixed-species planting, unevenly aged stand management, retention of legacy trees, and natural regeneration. Notably, this improvement does not require reductions in mean productivity. This aligns with emerging global evidence that structural complexity promotes ecosystem stability [7,29,36,43] and provides a mechanistic basis for climate-smart forest management that balances carbon accumulation with drought resilience.

5. Conclusions

Our study identified that canopy structural complexity, quantified by the Waveform Structural Complexity Index (WSCI) from 7,785,776 GEDI footprints across 338,598 forested 1 km grid cells in China, modulates the carbon–water trade-off: a spline-based model explained 81.7% of NPP variance ($R^2 = 0.817$), the P−ET × WSCI interaction was highly significant ($F = 92.0$, $p < 0.001$), and the marginal water sensitivity of NPP shifted from negative to positive with increasing complexity (−19.2, −9.2, and +8.2 g C m^{-2} yr^{-1} per standardized unit), while residual NPP–P−ET correlation remained near zero ($\rho = 0.0002$) and did not reverse across WSCI terciles or resolutions. These findings highlight that structural complexity strengthens the marginal water response of carbon uptake rather than merely buffering forests, operating through the mean response; therefore, promoting structurally complex forests can enhance the responsiveness of China's carbon sink to water without sacrificing mean productivity, supporting climate-smart forest management. Further studies are required to adopt explicit spatial correlation structures, broaden carbon indicators and hydrologically explicit water-availability metrics, and extend the analysis to other biomes to confirm the generality of this structure-mediated reversal.

Supplementary Materials: The following supporting information can be downloaded at: https://www.mdpi.com/article/10.3390/f17121421/s1; Figure S1: Spatial distribution of (a) PC1, (b) PC2, (c) PC3, (d) PC4, (e) elevation, (f) temperature, (g) solar radiation, (h) relative humidity, (i) VPD, (j) PDSI, and (k) soil moisture; Table S1: Descriptive statistics of variables used in the analysis.

Author Contributions: Conceptualization, G.L. and M.W.; methodology, X.S.; software, X.S.; validation, X.S., G.L., and M.W.; formal analysis, X.S.; investigation, X.S. and F.L.; resources, G.L.; data curation, F.L.; writing—original draft preparation, X.S. and M.W.; writing—review and editing, X.S., G.L., M.W., and F.L.; visualization, F.L.; supervision, M.W.; project administration, G.L.; funding acquisition, G.L. All authors have read and agreed to the published version of the manuscript.

Funding: This study was funded by the National Key Research and Development Program of China (Grant No. 2023YFF0805401), and the National Natural Science Foundation of China (Grant No. 42071373).

Data Availability Statement: The GEDI L4C Footprint Level Waveform Structural Complexity Index data are available at https://search.earthdata.nasa.gov/search (accessed on 17 June 2026). The forest aboveground biomass dataset is available via Zenodo at https://zenodo.org/records/12620984 (accessed on 19 June 2026). The forest age dataset is available at https://doi.org/10.6084/m9.figshare.24464170 (accessed on 25 June 2026). The NPP and Evapotranspiration dataset is available at https://glass.hku.hk/download.html (accessed on 7 May 2026). The

precipitation, temperature, downward shortwave radiation, and relative humidity datasets are available at https://www.tpdc.ac.cn/zh-hans/data/e60dfd96-5fd8-493f-beae-e8e5d24dece4 (accessed on 7 May 2026). The soil moisture, PDSI, and VPD datasets are available at https://www.climatologylab.org/terraclimate.html (accessed on 16 May 2026).

Conflicts of Interest: The authors declare no conflicts of interest.

Abbreviations

The following abbreviations are used in this manuscript:

GEDI	Global Ecosystem Dynamics Investigation
L4C	Level 4C
WSCI	Waveform Structural Complexity Index
FHD	Foliage height diversity
P−ET	Precipitation minus evapotranspiration
WA	Water availability
ET	Evapotranspiration
P	Precipitation
NPP	Net primary productivity
AGB	Aboveground biomass
PDSI	Palmer Drought Severity Index
VPD	Vapor pressure deficit
DEM	Digital elevation model

Appendix A

Specification of Equation (1)

For grid cell i, the model of Section 2.3.1 can be written in full as:

$$NPP_i = \beta_0 + \sum_{j=1}^{k_1} a_j b_j(z_{P-ET,i}) + \sum_{m=1}^{k_2} c_m b_m(z_{WSCI,i}) + \sum_{j=1}^{k_1}\sum_{m=1}^{k_2} d_{jm} b_j(z_{P-ET,i}) b_m(z_{WSCI,i}) + \sum_{p=1}^{3} \gamma_p PC_{p,i} + \sum_{q=1}^{k_3} e_q b_q(z_{DEM,i}) + g_1(x_i) + g_2(y_i) + \varepsilon_i$$

where NPP_i is the annual net primary productivity in grid cell i and β_0 is the model intercept; the index i runs over the 338,598 1 km grid cells retained for the analysis. $z_{P-ET,i}$, $z_{WSCI,i}$ and $z_{DEM,i}$ are the cell values of the annual water balance P−ET, of the WSCI and of elevation, each standardized to zero mean and unit variance before entry into the model, so that all spline coefficients below are expressed on a common scale.

$b_j(\cdot)$ and $b_m(\cdot)$ are the natural-cubic-spline basis functions of z_{P-ET} and z_{WSCI}, each evaluated at the value observed in cell i, and the same family of basis functions, indexed by q, is applied to z_{DEM}; the bases have interior knots at equally spaced quantiles of the observed distribution and linear tails beyond the boundary knots. a_j (j = 1, …, k_1) are the coefficients of the P−ET marginal basis, c_m (m = 1, …, k_2) those of the WSCI marginal basis, and e_q (q = 1, …, k_3) those of the elevation marginal basis, with $k_1 = k_2 = 8$ and $k_3 = 6$ being the basis dimensions, i.e., the number of basis functions and of coefficients of each term.

d_{jm} (j = 1, …, k_1; m = 1, …, k_2) are the coefficients of the interaction surface, which is the row-wise tensor product of the two marginal bases and therefore carries $k_1 \times k_2 = 64$ coefficients; the marginal bases used inside the interaction are the same functions as those used for the main effects, which is why the interaction does not refit them. $PC_{p,i}$ (p

= 1, 2, 3) is the score of the p-th principal component of the standardized environmental covariate block described in Section 2.3.1, and γ_p is its coefficient; only the first three components are retained.

$g_1(x_i)$ and $g_2(y_i)$ are smooth spatial-trend terms, i.e., univariate natural-cubic-spline bases of the Albers x and y coordinates of cell i with k = 12 basis functions and 12 coefficients each, which absorb broad-scale spatial structure that the covariates do not capture; ε_i is the residual error of cell i. Because no term of Equation (1) involves a product of more than two basis functions, the apparent complexity of the equation is a notational compression rather than a structural feature of the model.

References

1. Chang, Q.; Wang, L.; Barnes, M.L.; Ficklin, D.L.; Benson, M.C.; Novick, K.A. Widespread Increase in Global Plant Water Stress Obscured by Greening. *AGU Adv.* **2026**, *7*, e2025AV002243. https://doi.org/10.1029/2025AV002243.
2. Lan, X.; Liu, Z.; Chen, X.; Lin, K.; Cheng, L. Trade-off between Carbon Sequestration and Water Loss for Vegetation Greening in China. *Agric. Ecosyst. Environ.* **2021**, *319*, 107522. https://doi.org/10.1016/j.agee.2021.107522.
3. Hu, T.; Liu, X.; Wu, X.; Niu, C.; Su, Y. Advance in Forest Canopy Structural Complexity Research. *Natl. Remote Sens. Bull.* **2025**, *29*, 83–101.
4. Matsuo, T.; Martínez-Ramos, M.; Bongers, F.; Van Der Sande, M.T.; Poorter, L. Forest Structure Drives Changes in Light Heterogeneity during Tropical Secondary Forest Succession. *J. Ecol.* **2021**, *109*, 2871–2884. https://doi.org/10.1111/1365-2745.13680.
5. Ma, Q.; Su, Y.; Hu, T.; Jiang, L.; Mi, X.; Lin, L.; Cao, M.; Wang, X.; Lin, F.; Wang, B.; et al. The Coordinated Impact of Forest Internal Structural Complexity and Tree Species Diversity on Forest Productivity across Forest Biomes. *Fundam. Res.* **2024**, *4*, 1185–1195. https://doi.org/10.1016/j.fmre.2022.10.005.
6. Ehbrecht, M.; Schall, P.; Ammer, C.; Seidel, D. Quantifying Stand Structural Complexity and Its Relationship with Forest Management, Tree Species Diversity and Microclimate. *Agric. For. Meteorol.* **2017**, *242*, 1–9. https://doi.org/10.1016/j.agrformet.2017.04.012.
7. LaRue, E.A.; Knott, J.A.; Domke, G.M.; Chen, H.Y.; Guo, Q.; Hisano, M.; Oswalt, C.; Oswalt, S.; Kong, N.; Potter, K.M.; et al. Structural Diversity as a Reliable and Novel Predictor for Ecosystem Productivity. *Front. Ecol. Environ.* **2023**, *21*, 33–39. https://doi.org/10.1002/fee.2586.
8. Ogutu, B.O.; D'Adamo, F.; Dash, J. Impact of Vegetation Greening on Carbon and Water Cycle in the African Sahel-Sudano-Guinean Region. *Glob. Planet. Change* **2021**, *202*, 103524. https://doi.org/10.1016/j.gloplacha.2021.103524.
9. Hoek Van Dijke, A.J.; Herold, M.; Mallick, K.; Benedict, I.; Machwitz, M.; Schlerf, M.; Pranindita, A.; Theeuwen, J.J.E.; Bastin, J.-F.; Teuling, A.J. Shifts in Regional Water Availability Due to Global Tree Restoration. *Nat. Geosci.* **2022**, *15*, 363–368. https://doi.org/10.1038/s41561-022-00935-0.
10. Liu, Y.; Li, Z.; Chen, Y.; Jin, L.; Li, F.; Wang, X.; Long, Y.; Liu, C.; Kayumba, P.M. Global Greening Drives Significant Soil Moisture Loss. *Commun. Earth Environ.* **2025**, *6*, 600. https://doi.org/10.1038/s43247-025-02470-3.
11. Sun, W.; Zhou, S.; Yu, B.; Zhang, Y.; Keenan, T.; Fu, B. Soil Moisture-Atmosphere Interactions Drive Terrestrial Carbon-Water Trade-Offs. *Commun. Earth Environ.* **2025**, *6*, 169. https://doi.org/10.1038/s43247-025-02145-z.
12. Han, Q.; Ren, S.; Sun, H.; Guo, S.; Zhang, J.; Nan, J.; Han, W.; Ding, Y.; Peng, S. Global Ecological Restoration Framework Trading off Carbon Sequestration and Water Consumption. *Sci. China Earth Sci.* **2026**, *69*, 210–220. https://doi.org/10.1007/s11430-025-1729-3.
13. Wang, J.; Tong, X.; Wang, H.; Liu, S.; Zeng, J.; Xu, J.; Tian, Z.; You, Y.; Huang, X.; Huang, B.; et al. Tree Species Diversity and Structural Complexity Drive the Stability of Productivity in Subtropical Forest Restoration. *J. For. Res.* **2026**, *37*, 124. https://doi.org/10.1007/s11676-026-02071-6.
14. Liu, X.; Feng, Y.; Hu, T.; Luo, Y.; Zhao, X.; Wu, J.; Maeda, E.E.; Ju, W.; Liu, L.; Guo, Q.; et al. Enhancing Ecosystem Productivity and Stability with Increasing Canopy Structural Complexity in Global Forests. *Sci. Adv.* **2024**, *10*, eadl1947. https://doi.org/10.1126/sciadv.adl1947.
15. Crockett, E.T.H.; Atkins, J.W.; Guo, Q.; Sun, G.; Potter, K.M.; Ollinger, S.; Silva, C.A.; Tang, H.; Woodall, C.W.; Holgerson, J.; et al. Structural and Species Diversity Explain Aboveground Carbon Storage in Forests across the United States: Evidence from GEDI and Forest Inventory Data. *Remote Sens. Environ.* **2023**, *295*, 113703. https://doi.org/10.1016/j.rse.2023.113703.

16. Gong, C.; Tan, Q.; Liu, G.; Xu, M. Advantage of Mixed Trees in the Trade-off between Soil Water Storage and Tree Biomass: A Meta-Analysis from Artificially Planted Forests in Chinese Loess Plateau. *CATENA* **2022**, *214*, 106232. https://doi.org/10.1016/j.catena.2022.106232.
17. Su, Y.; Pu, J.; Huang, J.; Xing, Z.; Du, J.; Hong, Y.; Wang, X.; Wang, Y.; Liu, K. Species Richness Increases Vegetation Carbon Sequestration but Decreases Soil Carbon Storage in Temperate Grasslands of China. *Agric. Ecosyst. Environ.* **2026**, *406*, 110417. https://doi.org/10.1016/j.agee.2026.110417.
18. Torresani, M.; Moudry, V.; Hakkenberg, C.R.; Goetz, S.J.; Coomes, D.; Cotrina-Sanchez, A.; Armston, J.D.; Vogeler, J.C.; Roy, D.; Rocchini, D.; et al. The Role of GEDI Spaceborne Lidar in Biodiversity Analyses: A Topical Review. *Environ. Res. Lett.* **2026**, *21*, 093003. https://doi.org/10.1088/1748-9326/ae608a.
19. Schneider, F.D.; Ferraz, A.; Hancock, S.; Duncanson, L.I.; Dubayah, R.O.; Pavlick, R.P.; Schimel, D.S. Towards Mapping the Diversity of Canopy Structure from Space with GEDI. *Environ. Res. Lett.* **2020**, *15*, 115006. https://doi.org/10.1088/1748-9326/ab9e99.
20. Marselis, S.M.; Keil, P.; Chase, J.M.; Dubayah, R. The Use of GEDI Canopy Structure for Explaining Variation in Tree Species Richness in Natural Forests. *Environ. Res. Lett.* **2022**, *17*, 045003. https://doi.org/10.1088/1748-9326/ac583f.
21. De Conto, T.; Armston, J.; Dubayah, R. Characterizing the Structural Complexity of the Earth's Forests with Spaceborne Lidar. *Nat. Commun.* **2024**, *15*, 8116. https://doi.org/10.1038/s41467-024-52468-2.
22. De Conto, T.; Armston, J.; Dubayah, R.O. GEDI L4C Footprint Level Waveform Structural Complexity Index, Version 3. 2026. Available online: https://www.earthdata.nasa.gov/data/catalog/ornl-cloud-gedi-l4c-wsci-v3-2520-3 (accessed on 1 June 2026).
23. Oliveira, P.V.C.; Zhang, X.; Peterson, B.; Ometto, J.P. Using Simulated GEDI Waveforms to Evaluate the Effects of Beam Sensitivity and Terrain Slope on GEDI L2A Relative Height Metrics over the Brazilian Amazon Forest. *Sci. Remote Sens.* **2023**, *7*, 100083. https://doi.org/10.1016/j.srs.2023.100083.
24. Feyen, J.; Wortel, V.; Calders, K.; Armston, J.; Vancoillie, F. Characterizing Mangrove Forest Succession in Suriname Using GEDI Waveform Metrics. *Remote Sens. Environ.* **2026**, *334*, 115244. https://doi.org/10.1016/j.rse.2026.115244.
25. He, J.; Yang, K.; Tang, W.; Lu, H.; Qin, J.; Chen, Y.; Li, X. The First High-Resolution Meteorological Forcing Dataset for Land Process Studies over China. *Sci. Data* **2020**, *7*, 25. https://doi.org/10.1038/s41597-020-0369-y.
26. Wang, G.; Jing, C.; Yuan, X.; Dong, P.; Shao, Y.; Shi, M.; Dong, T. Vegetation Greening Decouples Terrestrial Carbon–water Cycles through Contrasting Effects on Water Availability. *GISci. Remote Sens.* **2026**, *63*, 2697122. https://doi.org/10.1080/15481603.2026.2697122.
27. Zhang, Y.; Li, C.; Chiew, F.H.S.; Post, D.A.; Zhang, X.; Ma, N.; Tian, J.; Kong, D.; Leung, L.R.; Yu, Q.; et al. Southern Hemisphere Dominates Recent Decline in Global Water Availability. *Science* **2023**, *382*, 579–584. https://doi.org/10.1126/science.adh0716.
28. Cai, Y.; Zhu, P.; Li, X.; Liu, X.; Chen, Y.; Shen, Q.; Xu, X.; Zhang, H.; Nie, S.; Wang, C.; et al. Dynamics of China's Forest Carbon Storage: The First 30 m Annual Aboveground Biomass Mapping from 1985 to 2023. *Earth Syst. Sci. Data* **2025**, *17*, 6993–7018. https://doi.org/10.5194/essd-2025-96.
29. Yi, X.; Vincent, G.; Hu, T.; Liu, J.; Lutz, J.; Ren, H.; Chen, L.; Burslem, D.; Birch, J.; Cao, M.; et al. Canopy Structural Diversity Mediates the Effect of Climate on Primary Productivity in Forests. *Nat. Commun.* **2026**, *17*, 8552. https://doi.org/10.1038/s41467-026-75043-3.
30. Toda, M.; Knohl, A.; Luyssaert, S.; Hara, T. Simulated Effects of Canopy Structural Complexity on Forest Productivity. *For. Ecol. Manag.* **2023**, *538*, 120978. https://doi.org/10.1016/j.foreco.2023.120978.
31. Dănescu, A.; Albrecht, A.T.; Bauhus, J. Structural Diversity Promotes Productivity of Mixed, Uneven-Aged Forests in Southwestern Germany. *Oecologia* **2016**, *182*, 319–333. https://doi.org/10.1007/s00442-016-3623-4.
32. Fahey, C.; Choi, D.; Wang, J.; Domke, G.M.; Edwards, J.D.; Fei, S.; Kivlin, S.N.; LaRue, E.A.; McCormick, M.K.; McShea, W.J.; et al. Canopy Complexity Drives Positive Effects of Tree Diversity on Productivity in Two Tree Diversity Experiments. *Ecology* **2025**, *106*, e4500. https://doi.org/10.1002/ecy.4500.
33. Messier, C.; Bauhus, J.; Sousa-Silva, R.; Auge, H.; Baeten, L.; Barsoum, N.; Bruelheide, H.; Caldwell, B.; Cavender-Bares, J.; Dhiedt, E.; et al. For the Sake of Resilience and Multifunctionality, Let's Diversify Planted Forests! *Conserv. Lett.* **2022**, *15*, e12829. https://doi.org/10.1111/conl.12829.
34. Atkins, J.W.; Shiklomanov, A.; Mathes, K.C.; Bond-Lamberty, B.; Gough, C.M. Effects of Forest Structural and Compositional Change on Forest Microclimates across a Gradient of Disturbance Severity. *Agric. For. Meteorol.* **2023**, *339*, 109566. https://doi.org/10.1016/j.agrformet.2023.109566.
35. Meng, Z.; Liu, J.; Cao, L.; Li, B.; Wang, N.; Chen, M.; Zhou, Z. Trade-off between Soil Carbon and Water Following Revegetation across Climatic Gradients on the Loess Plateau. *CATENA* **2025**, *255*, 109071. https://doi.org/10.1016/j.catena.2025.109071.

36. Crockett, E.T.H.; Guo, Q.; Atkins, J.W.; Sun, G.; Potter, K.M.; Costanza, J.K.; Ollinger, S.V.; Woodall, C.W.; McNulty, S.; Trettin, C.; et al. Influences of Structural and Species Diversity on Forest Resistance to Drought. *Ecol. Lett.* **2026**, *29*, e70351. https://doi.org/10.1111/ele.70351.
37. Neumann, R.B.; Cardon, Z.G. The Magnitude of Hydraulic Redistribution by Plant Roots: A Review and Synthesis of Empirical and Modeling Studies. *New Phytol.* **2012**, *194*, 337–352. https://doi.org/10.1111/j.1469-8137.2012.04088.x.
38. Zhang, A.; Yu, H.; Cheng, C.; Guo, H.; He, N. Structural Diversity Surpasses Species Diversity in Regulating the Spatial Variation of Grassland Productivity. *J. Ecol.* **2026**, *114*, e70294. https://doi.org/10.1111/1365-2745.70294.
39. Stephenson, N.L.; Das, A.J.; Condit, R.; Russo, S.E.; Baker, P.J.; Beckman, N.G.; Coomes, D.A.; Lines, E.R.; Morris, W.K.; Rüger, N.; et al. Rate of Tree Carbon Accumulation Increases Continuously with Tree Size. *Nature* **2014**, *507*, 90–93. https://doi.org/10.1038/nature12914.
40. Zhang, Y.; Zou, Y.; Wang, Y. Remote Sensing of Forest Above-Ground Biomass Dynamics: A Review. *Forests* **2025**, *16*, 821. https://doi.org/10.3390/f16050821.
41. Hao, W.; Bu, X.; Chen, J.; Li, Z.; Li, B. Trade-off Between Soil Water Maintenance and Carbon Sequestration During the Implementation of Ecological Restoration Programs in the Semi-Arid Loess Plateau. *Forests* **2025**, *16*, 657. https://doi.org/10.3390/f16040657.
42. Zhang, J.; Zhang, Y.; Wang, X.; He, T.; Xia, H.; Zhang, K.; Zhang, Q. National Forest Restoration Projects in China: Cost-Efficiency, and Trade-Off Between Carbon Sequestration and Water Consumption. *Earth's Future* **2024**, *12*, e2024EF004976. https://doi.org/10.1029/2024EF004976.
43. Park, M.H.; Guzmán Q., J.A.; Dyalsingh, H.; Scott, A.; Cavender-Bares, J. Forest Composition and Diversity Buffer Microclimates and Enhance Productivity. *J. Ecol.* **2026**, *114*, e70347. https://doi.org/10.1111/1365-2745.70347.

Disclaimer/Publisher's Note: The statements, opinions and data contained in all publications are solely those of the individual author(s) and contributor(s) and not of MDPI and/or the editor(s). MDPI and/or the editor(s) disclaim responsibility for any injury to people or property resulting from any ideas, methods, instructions or products referred to in the content.